

Sucrose-Mediated Fast Synthesis of Zinc Oxide Nanoparticles for the Photocatalytic Degradation of Organic Pollutants in Water

Md. Tariqul Islam,^{*,†,‡,§} Ariana Dominguez,[†] Bonifacio Alvarado-Tenorio,[§] Ricardo A. Bernal,[†] Milka O. Montes,^{||} and Juan C. Noveron^{*,†,‡,§}

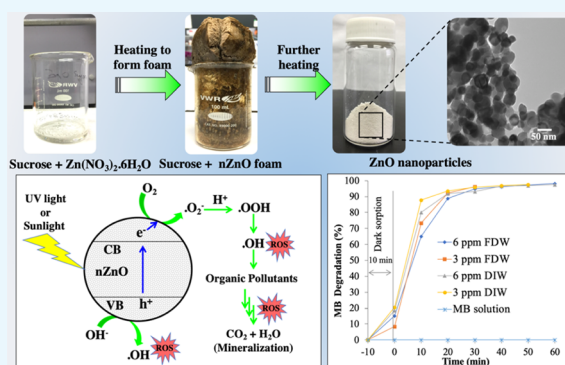
[†]Department of Chemistry, University of Texas, El Paso, 500 West University Avenue, El Paso, Texas 79968, United States

[‡]Nanosystems Engineering Research Center for Nanotechnology-Enabled Water Treatment (NEWT), Rice University, 6100 Main Street, MS 6398, Houston, Texas 77005, United States

[§]Instituto de Ciencias Biomédicas, Universidad Autónoma de Ciudad Juárez, Ciudad Juárez, Chihuahua 32315, Mexico

^{||}Department of Chemistry, University of Texas, Permian Basin, 4901 E University Blvd, Odessa, Texas 79762, United States

ABSTRACT: We report a facile method for the synthesis of zinc oxide nanoparticles (nZnOs) by rapidly heating a paste of zinc nitrate and sucrose on the hot plate at 500 °C. The transmission electron microscopy images revealed the spherical shape of the nZnO with an average size of 35 nm. The band gap and the specific surface area of the nZnO were measured to be about 3.32 eV and 80.11 m²/g, respectively. The nZnO was utilized for the photocatalytic degradation of methyl orange (MO) and methylene blue (MB) in water under the ultraviolet (UV-B) light and sunlight irradiation. Photocatalysis was performed in two types of water matrices, viz., the deionized water and the simulated fresh drinking water. Almost a complete degradation of MO and MB was obtained within 30 min of UV-B light irradiation. Under sunlight irradiation, more than 95% of the MO solution underwent degradation within 30 min. The photocatalytic stability of the nZnO was examined for five cycles, and a similar activity was found throughout the cycles. The photocatalytic generation of the hydroxyl radical ([•]OH) was confirmed by the terephthalic acid photoluminescence tests. Moreover, the synthesis methodology was validated by triplicating the nZnO synthesis. Every time, the nZnO demonstrated a similar photocatalytic activity, which confirmed the robustness of the synthesis procedure.



1. INTRODUCTION

Zinc oxide (ZnO) is one of the most extensively studied semiconductor-type metal oxides.¹ As a semiconductor material, ZnO has wide-band gap of 3.37 eV and an exciton binding energy of 60 meV.² In addition to the semiconductor property, ZnO has intriguing piezoelectric,³ oxidizing,⁴ and antibacterial properties.^{5–7} Moreover, because of the cheaper price, abundance, and high chemical, as well as physical robustness, ZnO is widely used in a number of applications. For example, ZnO is used in transparent electrodes of the dye-sensitized solar cells,⁸ piezoelectric nanogenerators,⁹ sensing,¹⁰ as fillers in numerous products,¹¹ ultraviolet (UV) light absorbers in personal care products,¹² light-emitting diodes,¹³ UV photodetectors,¹⁴ and photocatalysis.^{15–18} As a photocatalyst, ZnO and its nanocomposites demonstrate excellent ability toward the degradation of organic pollutants in water under the UV light illumination.^{19–23} Organic pollutants undergo degradation on the ZnO surface through the redox processes driven by the electronic excitation between valence and conduction bands (CBs).²⁴ Also, ZnO has the ability to generate reactive oxygen species (ROS) under the UV light

irradiation, which can degrade organic pollutants and inactivate or inhibit microorganisms in water.

Recently, the photocatalytic degradation of organic pollutants has drawn tremendous attention because of its advantages over other methods, viz., adsorption, precipitation, filtration, coagulation, biological treatment, and so forth.²⁵ For instance, photocatalytic processes usually do not require chemicals and do not produce any secondary pollutants; photocatalytic processes have the ability to degrade hazardous organic pollutants to mineralization, whereas most of the other techniques transfer pollutants from one place to another.²⁶ Moreover, the photocatalyst can be used for multiple cycles without the loss of the activity. As ZnO demonstrates excellent photocatalytic activity, it could potentially be used as an efficient and viable photocatalyst for the degradation of organic pollutants in water. However, the photocatalytic activity of ZnO is obtained when the particles are in the nanoscopic size range (1–100 nm) in contrast to the macroscopic or bulk size.

Received: January 3, 2019

Accepted: February 13, 2019

Published: April 10, 2019

Therefore, there is a need for the synthesis of high-quality zinc oxide nanoparticles (nZnOs) via a facile method that avoids the use of harsh chemicals and rigorous experimental procedures.

Various chemical and physical methods have been reported for the synthesis of nZnO thus far.²⁷ Some of the commonly employed methods include the sol–gel,^{28,29} combustion,^{30,31} hydro/solvothermal,^{32–35} laser ablation,³⁶ chemical vapor deposition,³⁷ microemulsion techniques,³⁸ and the microwave-assisted synthesis.³⁹ In addition, there are physical top-down techniques, such as mechanical or mechanochemical milling, where the bulk ZnO is converted into nZnO.⁴⁰ A large number of methods for the synthesis of nZnO require expensive and hazardous substrates, rigorous experimental conditions, tedious techniques, and sophisticated instruments. Moreover, sometimes, the nZnOs are not efficient enough for the desired photocatalytic applications. Therefore, it is important to develop a simple, fast, and low-cost method for the synthesis of high-quality and photocatalytically active nZnO. Recently, the combustion synthesis has become a very popular and effective technique to synthesize metal oxide nanoparticles because of the versatility, simplicity, and rapidity of the process.⁴¹ In combustion synthesis, a mixture of metal salt as an oxidizer (e.g., metal nitrates) and fuels (e.g., urea, glycine, and hydrazides) is heated to a high temperature. When heated to a temperature, the mixture undergoes a self-sustained reaction to produce uniform metal oxide nanoparticles while burning away the fuel in the form of CO₂, H₂O, and other gases. Utilizing the combustion synthesis technique, many types of single and mixed metal oxide nanoparticles have been prepared.^{42,43} For the synthesis of nZnO, different types of organic compounds and plant extracts have been used as fuels.⁴⁴ However, there are some drawbacks of these methods. For example, the plant extracts containing metallic and nonmetallic impurities can modify the desired properties of the nZnO by doping it with the metallic and nonmetallic elements. Also, the utilization of plant extracts for the large-scale synthesis of engineered nanoparticles may not be a viable method, and it is still under questions.⁴⁵ Other organic compounds, such as urea and thiourea, usually make nZnO doped with nitrogen and sulfur, which may be undesired and can alter the desired catalytic property of the nZnO. Therefore, for the preparation of high-quality nZnO through the combustion synthesis method, a highly pure and cheap fuel is necessary. In this regard, sucrose could potentially be used as a fuel because of its low price and availability in the form of high purity. To the best of our knowledge, there is no report for the synthesis of nZnO utilizing sucrose as the fuel in the combustion synthesis. Additionally, there is no report for the synthesis of nZnO that can be completely performed using a hot plate within 30 min period of time.

Herein, we report a simple and fast method for the synthesis of nZnO by rapidly heating a paste of zinc nitrate hexahydrate [Zn(NO₃)₂·6H₂O] and sucrose (C₁₂H₂₂O₁₁) at 500 °C on the hot plate. The as-synthesized nZnO was thoroughly characterized by the high-resolution transmission electron microscopy (HRTEM), scanning electron microscopy (SEM), energy-dispersive X-ray spectroscopy (EDX), X-ray powder diffraction spectroscopy (XRPD), X-ray photoelectron spectroscopy (XPS), UV–visible absorption spectroscopy, Brunauer–Emmett–Teller (BET) surface area analysis, and Fourier transform infrared spectroscopy (FTIR). The nZnO demonstrated very good performance toward the photocatalytic

degradation organic pollutants, viz., methyl orange (MO) and methylene blue (MB), in water under the UV-B light and sunlight irradiation. The photocatalytic generation of hydroxyl radical (*OH) was confirmed through the terephthalic acid (TA) photoluminescence (PL) tests. The reproducibility of the synthesis method and the stability of the nZnO were also studied to evaluate the potential application of the nZnO for the photocatalytic water treatment.

2. MATERIALS AND METHODS

2.1. Materials. Unless otherwise mentioned, all chemicals were used as received. Sucrose (C₁₂H₂₂O₁₁ > 99.5%), zinc nitrate hexahydrate [Zn(NO₃)₂·6H₂O ≥ 98%], sodium hydroxide (NaOH ≥ 98%), and TA [C₈H₆O₄ = 98%] were purchased from Sigma-Aldrich. MO (C₁₄H₁₅N₃O₃S > 98.0%) and MB (C₁₆H₁₈ClN₃S > 98%) were obtained from TCI America and Consolidated Chemical, respectively. A Fisher Scientific 11-600-49sh Isotemp Analog Hot Plate Stirrer was used as the heating source for the synthesis of nZnO. Throughout the nZnO synthesis period, the hot plate was preheated to its highest capacity and the hot plate surface temperature was measured to be about 500 °C. An UV box reactor (UVP Ultraviolet Cross-linker, model CL-1000), having UV-B fluorescent tube lamps, was used for the photocatalytic degradation of MO and MB. The UV reactor shined the light from the top only. The intensity of light on the surface of the reaction was measured to be 21 500 lux. The intensity of light was measured by using a digital Light Meter LX1330B. The UV-B lamp generated light of 302 nm wavelength, as specified by the vendor of the lamp. Syringe filters with polypropylene housing and PTFE membrane material with 0.45 μm pore size were obtained from VWR, which were used to filter the reaction mixture. Milli-Q water (>18.20 MΩ cm resistivity) was obtained from the Milli-Q (Advantage A-10) water filter system. The simulated fresh drinking water (FDW) was prepared following the Nanotechnology Enabled Water Treatment (NEWTE) protocol. In detail, 252 mg/L NaHCO₃, 147 mg/L CaCl₂·2H₂O, 124 mg/L MgSO₄·7H₂O, 95 mg/L Na₂SiO₃·9H₂O, 12 mg/L NaNO₃, 2.2 mg/L NaF, and 0.18 mg/L NaH₂PO₄·H₂O were dissolved in the deionized water (DIW) to achieve the simulated FDW.

2.2. Characterization Techniques. UV–vis spectra were obtained by using an Agilent Cary 50 Conc UV–visible spectrophotometer. A quartz cuvette of 10 mm path length was used as the sample holder for the UV–vis studies. Solid-state UV–vis absorption spectroscopy of the nZnO thin film was carried out with the aid of the same UV–visible spectrophotometer. A thin film of nZnO was formed on the microscopic glass slide to obtain the solid-state UV–vis spectra. A paste of nZnO was prepared in ethanol using liquid hand soap as the surfactant. A thin film of nZnO was formed on a glass slide by the doctor blading technique. The wet thin film on the glass slide was then heated on a hot plate at 500 °C for about 30 min to burn off the surfactant and any other organic impurities. Afterward, the hot plate was turned off to cool it down under the ambient conditions. For the UV–vis spectra of the nZnO suspension, a suspension of nZnO in ethanol (0.125 mg nZnO/mL) was prepared by bath sonication. Transmission electron microscopy (TEM) and HRTEM experiments were performed using a Hitachi H-7650 and JEOL JEM3200FS microscope, respectively. Acceleration voltages of 80 and 300 kV were used for the Hitachi H-7650 and JEOL JEM3200FS microscope, respectively. Carbon-film copper grids with 200

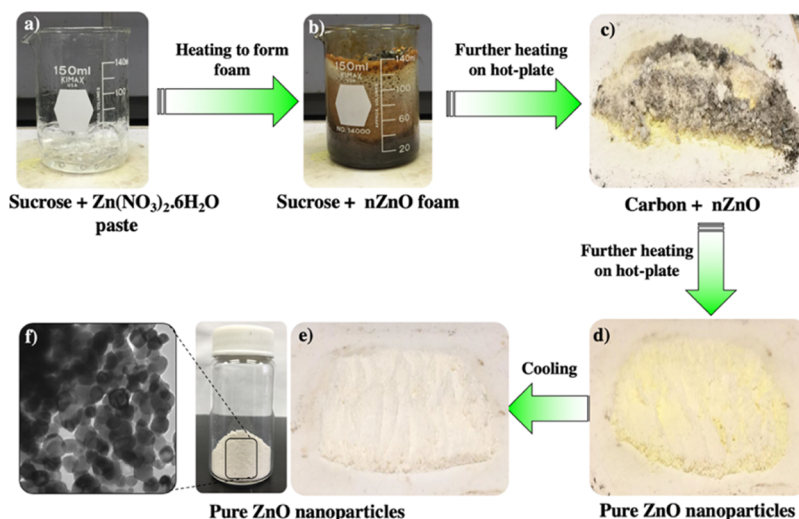


Figure 1. Scheme showing different stages for the synthesis of nZnO. (a) Viscous mixture of zinc nitrate and sucrose; (b) zinc nitrate decomposition into a foam-like structure of ZnO decomposed sucrose; (c,d) further heating of the foam at the hot plate to burn away the carbon; (d,e) pure nZnO when hot and after cooling; and (f) nZnO in a vial and a typical TEM image of the nZnO.

mesh (Electron Microscopy Sciences) were used for TEM imaging. For the TEM imaging, a suspension of the nZnO in ethanol (0.125 mg nZnO/mL) was prepared by bath sonication and a drop of this suspension was deposited onto the grid and air-dried before imaging. SEM image and the EDX experiments were carried out using a Hitachi S-3400N Type II scanning electron microscope (SEM) equipped with an energy-dispersive X-ray spectrometer. A carbon tape was used as the substrate for the SEM imaging. The XRPD spectrum was obtained by using a Bruker D8 DISCOVER X-ray diffractometer with Cu $K\alpha$ radiation ($\lambda = 0.15418$ nm). A Micromeritics ASAP 2020 surface area and porosity analyzer was used for the nitrogen adsorption isotherms and to obtain the specific surface area of the nZnO.

2.3. Synthesis of nZnO. A Fisher Scientific 11-600-49sh Isotemp Analog Hot Plate Stirrer was used as the heating source for the synthesis of nZnO. Throughout the nZnO synthesis period, the hot plate was preheated to its highest capacity. Although the hot plate was heated to its highest capacity, the temperature was measured to be about 500 °C at the surface of the hot plate. In detail, in a 150 mL glass beaker (Kimax), 1200 mg (3.51 mmol) of sucrose and 3569.88 mg (12 mmol) of $Zn(NO_3)_2 \cdot 6H_2O$ salt were mixed with 3 mL of DIW. The beaker was put on the preheated hot plate. Within 1–2 min, the mixture turned into a viscous solution and immediately after the viscous solution started to decompose generating brownish yellow gases. After 3–4 min, a blackish brown foam was obtained from the decomposition of zinc nitrate salt. Because the decomposition of zinc nitrate salt formed NO_2 and NO_x gases, the hot plate was placed in a fume hood with proper ventilation. Afterward, the blackish brown hot foam/powder was transferred from the beaker to the same bare hot plate. The powder was stirred by a spatula. While heating at this high temperature in air, the blackish powder turned into yellowish-white powder of nZnO. The carbon in the powder combusted away in the form of carbon dioxide. After 20 min of heating on the hot plate, the nZnO powder was allowed to cool down. For cooling, the hot plate was turned off and normal ambient cooling was utilized. The amount of nZnO obtained was about 810 mg, which was

stored under ambient condition for the characterization as well as the photocatalytic applications.

2.4. MO and MB Photodegradation Experiment.

Photocatalytic degradation of MO and MB was carried out in a glass beaker (Pyrex) with 150 mL of capacity and dimensions of diameter \times height = 28 mm \times 98 mm. MO and MB solutions having the concentrations of 3 and 6 ppm (mg/L) were used for the photocatalytic experiments, respectively. In the photodegradation experiments, 25 mg of the catalyst was homogeneously dispersed in 25 mL of MO or MB solution by 10 min of bath sonication in dark. The bath sonication facilitated the homogeneous dispersion of the nZnO as well as helped in the establishment of the adsorption–desorption equilibrium between the nZnO and the dye. The mixture was illuminated under the UV-lamps in the box reactor while stirring the mixture. At a regular interval of 5 min, 1 mL of the sample was withdrawn and filtered through a syringe filter for UV–vis spectroscopic analysis. The characteristic absorption maxima of MO and MB centered at 464 nm and 665 were used for the calculation of percent degradation, respectively. Same experimental conditions were utilized for the photocatalysis of MO under the sunlight illumination. Direct sunlight was utilized for the photocatalysis of MO in deionized and FDW matrices. For the cyclic stability experiments, the catalyst used in the first cycle was centrifuged and used in the same way for the subsequent cycles for the degradation of MO. The sample was taken from the centrifuged (4000 rpm, 5 min) supernatant so as to minimize the loss of the catalyst.

2.5. TA PL Test for the Detection of Hydroxyl Radicals.

The detail experimental procedure was similar to that of the photocatalytic MO or MB degradation tests. In this case, 25 mL of 5×10^{-3} M sodium terephthalate solution was used instead of the MO or MB solution. A stock solution of 5×10^{-3} M sodium terephthalate was prepared by the reaction of a required amount of TA with stoichiometric amount of NaOH in water. In every 5 min, 1 mL of the sample was withdrawn and filtered through the syringe filter. The fluorescence spectroscopy was carried out on the filtrate with an excitation wavelength of 315 nm to determine the fluorescence emission intensity of hydroxy terephthalate at 425 nm.

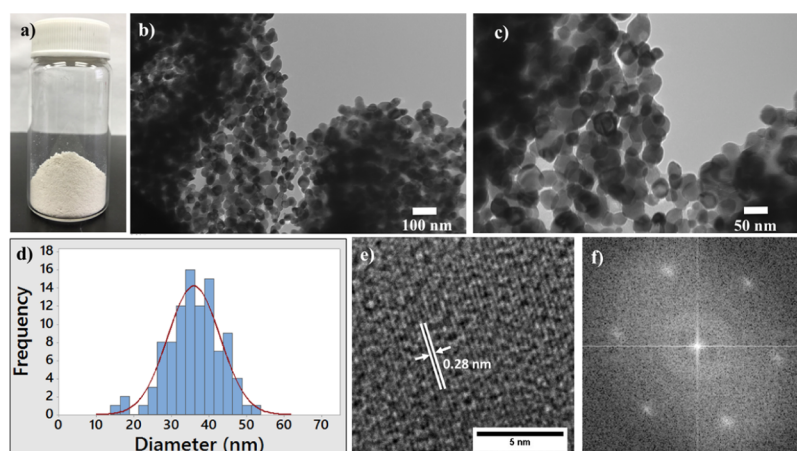
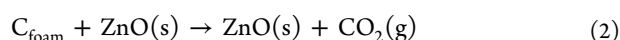
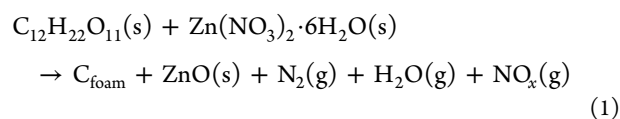


Figure 2. (a) Digital photograph of the nZnO in a glass vial; (b,c) TEM images of nZnO with varying magnifications; (d) size distribution of the nZnO based on the TEM image; (e) HRTEM image of the nZnO showing the crystalline structure of the (100) lattice plane; and (f) FFT image of the nZnO obtained from the HRTEM image.

3. RESULTS AND DISCUSSION

Because of the versatile applications of nZnO, there is a need for the synthesis of high-quality nZnO employing a simple and fast method. This report demonstrates a fast method for the preparation of photocatalytically active nZnO by rapidly heating a paste of $\text{Zn}(\text{NO}_3)_2 \cdot 6\text{H}_2\text{O}$ and sucrose at 500°C on the hot plate (Figure 1). On the basis of the previous studies, the proposed mechanism for the formation of nZnO can be explained as follows:⁴⁶ while heating on the hot plate, the mixture of $\text{Zn}(\text{NO}_3)_2 \cdot 6\text{H}_2\text{O}$ and sucrose dissolves and becomes concentrated to form a uniform viscous paste (Figure 1a). While further heating, the $\text{Zn}(\text{NO}_3)_2 \cdot 6\text{H}_2\text{O}$ starts to decompose rapidly to form NO_2 (brownish gas), N_2 , CO_2 , H_2O , and other nitrogenous gases, which blow the melted viscous paste and cause it to swell to form the blackish brown color foam (Figure 1b). Meanwhile, the sucrose undergoes partial carbonization through the dehydration and polymerization. The resulting foam-like composite is considered to contain nZnO embedded in a partially carbonized sucrose foam, eq 1.³⁷



Further heating of this partially carbonized foam with the embedded nZnO at elevated temperature causes the oxidation of the carbon to CO_2 leaving nZnO (eq 2, Figure 1c–e). It was observed that the nZnO looked yellowish white (Figure 1d) in color when hot and it turned to white when cooled down to room temperature (Figure 1e). Because of the oxygen vacancies in the ZnO crystal, when hot, it appears the color yellowish white and when cooled down to the room temperature, it appears white color because of the filling up of the oxygen vacancy. The advantage of the method is that the experimental conditions are simple, fast, and scalable. Moreover, the methodology does not require any expensive or hazardous reagents. The method can potentially be adapted to prepare a wide variety of other metal and mixed oxide nanoparticles.

The rapid industrialization and increasing population growth are posing a continual threat to the environment by polluting the air, water, and soil with numerous organic and inorganic contaminants. In regard to the aquatic environment, freshwater sources are being contaminated with numerous organic pollutants that are reported to be toxic, carcinogenic, and mutagenic to human beings and aquatic organisms. As a result, freshwater is not only becoming increasingly scarce but also hazardous to human health almost everywhere in the world. The utilization of nZnO for the photocatalytic degradation of organic pollutants in water could be considered as a viable and sustainable method for the purpose of water treatment. Therefore, a facile synthesis method of nZnO, as reported in this study, could accelerate the overall photocatalytic water treatment processes.

3.1. TEM and HRTEM Images of the nZnO. TEM images were obtained to visualize the size, shape, and the dispersity of the as-synthesized nZnO. The TEM images (Figure 2b,c) revealed that the nZnOs are predominantly spherical in shape and highly monodisperse with the smooth surface. It could be observed that the nZnO tended to aggregate, which could be attributed to the high surface area of nZnO.⁴⁷ The size distribution histogram, obtained by measuring the size of more than 100 randomly picked nanoparticles by the ImageJ software, demonstrated that the nZnOs have an average size of about 35 nm (Figure 2d). Although the size of the nZnO varied from 15 to 55 nm, the majority of the particles was in the size range of 32–40 nm. A digital photograph of the nZnO is shown in Figure 2a.

The crystalline nature of the nZnO was further analyzed by the HRTEM (Figure 2e). Clear lattice fringes can be seen, which indicates the highly crystalline structure of the nZnO. The interplanar spacing of 2.8 Å further corresponds to the (100) lattice plane of the nZnO.⁴⁸ The crystalline nature of the nZnO surface was also characterized by the fast Fourier transformation (FFT) analysis obtained from the HRTEM image of the nZnO (Figure 2f). The FFT analysis not only confirmed a good crystallinity but also determined the hexagonal wurtzite-type crystalline structure of the nZnO.^{49,50}

3.2. SEM Image and the EDX Spectrum of the nZnO. The morphology and the elemental composition of the as-prepared nZnO were further studied by the SEM image and EDX spectrum (Figure 3), respectively. As shown in Figure 3a,

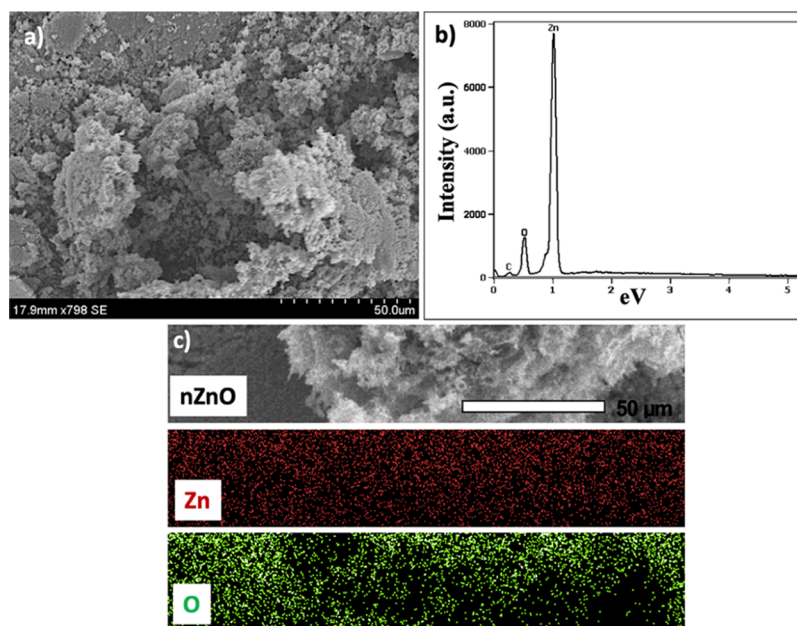


Figure 3. (a) Typical SEM image of the nZnO, (b) EDX spectra of the nZnO showing the elemental composition, and (c) SEM backscattered electron image of the nZnO and the zinc and oxygen X-ray EDS mapping.

the nZnO particles were seen to be aggregated with powder-like morphology. A porous morphology of the nZnO was also found from the SEM image.

To determine the qualitative information of the nZnO, the EDX spectrum was obtained (Figure 3b). The EDX spectrum generated strong peaks corresponding to zinc and oxygen, indicating a high purity of the as-synthesized nZnO. A small peak corresponding to carbon originated from the carbon tape that was used as the substrate for the analysis. The SEM backscattered electron image of the nZnO and the X-ray EDS elemental mapping image of the nZnO are shown in Figure 3c. As the EDS spectral analysis, the EDS elemental mapping image showed the presence and abundance of zinc and oxygen in the nZnO sample. This further confirmed the purity of the nZnO that was synthesized in this report.

3.3. XRPD Pattern and the BET Surface Area of the nZnO. The XRPD spectrum was obtained to determine the crystalline properties as well as the crystallite particle size of the nZnO. As shown in Figure 4, the diffraction pattern and the sharp peaks clearly indicate the crystalline nature of the as-prepared nZnO. Moreover, the diffraction peaks at $2\theta =$

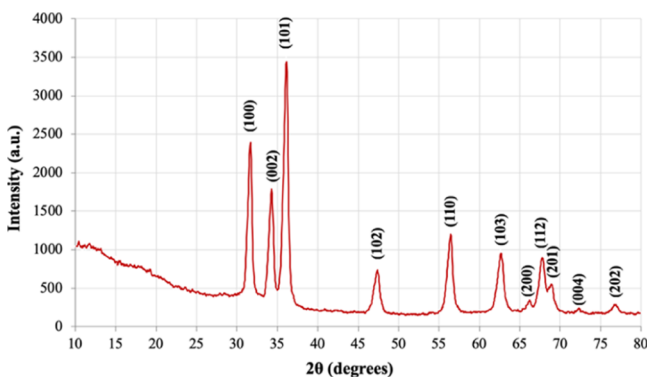


Figure 4. XRPD patterns showing the hexagonal wurtzite crystal structure of the nZnO.

31.66° , 34.20° , 36.10° , 47.36° , 56.47° , 62.63° , 66.20° , 67.81° , 68.99° , 72.40° , and 76.90° are characteristic to the (100), (002), (101), (102), (110), (103), (200), (112), (201), (004), and 202 lattice planes of the nZnO, respectively.^{51,52} This type of XRPD pattern is characteristic to the polycrystalline hexagonal wurtzite crystal structure of the nZnO (zincite, JCPDS 5-0664).⁵³ From the XRPD pattern, it could be observed that the intensity of the ZnO (101) diffraction peak is somewhat stronger than the other peaks. This indicates that the nZnOs have a preferential orientation toward (101) crystallographic direction.⁵⁴ The absence of any other undesired peaks in the XRPD pattern indicates the high purity of the nZnO, which is also confirmed by the EDX elemental analysis.⁵⁵

The average crystallite size of nZnO was further calculated by utilizing the Debye–Scherrer's formula (eq 3) from the XRD peak width of (101).⁵⁶

$$d = k\lambda/\beta \cos(\theta) \quad (3)$$

where d is the crystallite size, k is the shape factor (0.9), λ is the wavelength of Cu $K\alpha$ X-ray radiation (1.54 Å), θ is the Bragg diffraction angle, and β is the full width at half-maximum of the respective diffraction peak. Applying the Debye–Scherrer formula, the average crystallite size of the nZnO was found to be 28.9 nm. The crystallite size, obtained from the XRPD analysis, was found to have somewhat deviated from the average particle size measured by the TEM analysis. The crystallite size, measured from the XRPD analysis, is assumed to be the size of a coherently diffracting domain, and it is not necessarily the same as the particle size determined from the TEM images.

The nZnO was further characterized by the nitrogen gas adsorption studies to obtain the specific surface area, pore size, and the pore volume. The BET specific surface area of the nZnO was measured to be about 80.11 m²/g, which is comparable or higher than the reported values.^{57,58} Additionally, the Barrett–Joyner–Halenda pore volume and pore

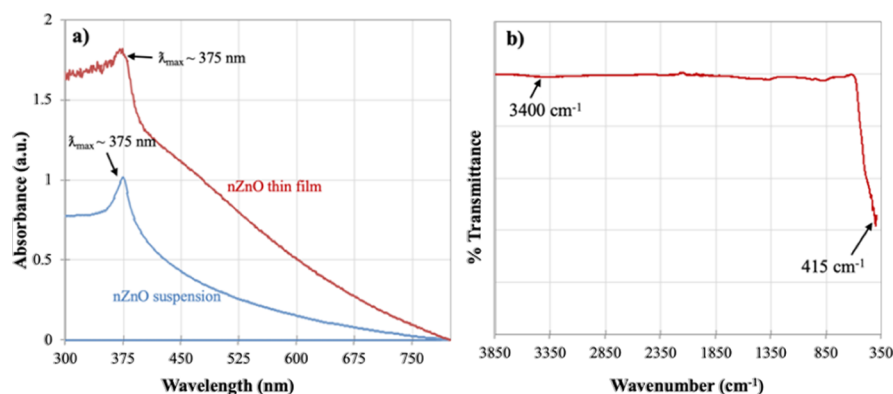


Figure 5. (a) UV–visible absorption spectra of the nZnO thin film and nZnO suspension in ethanol and (b) FTIR spectrum of the nZnO.

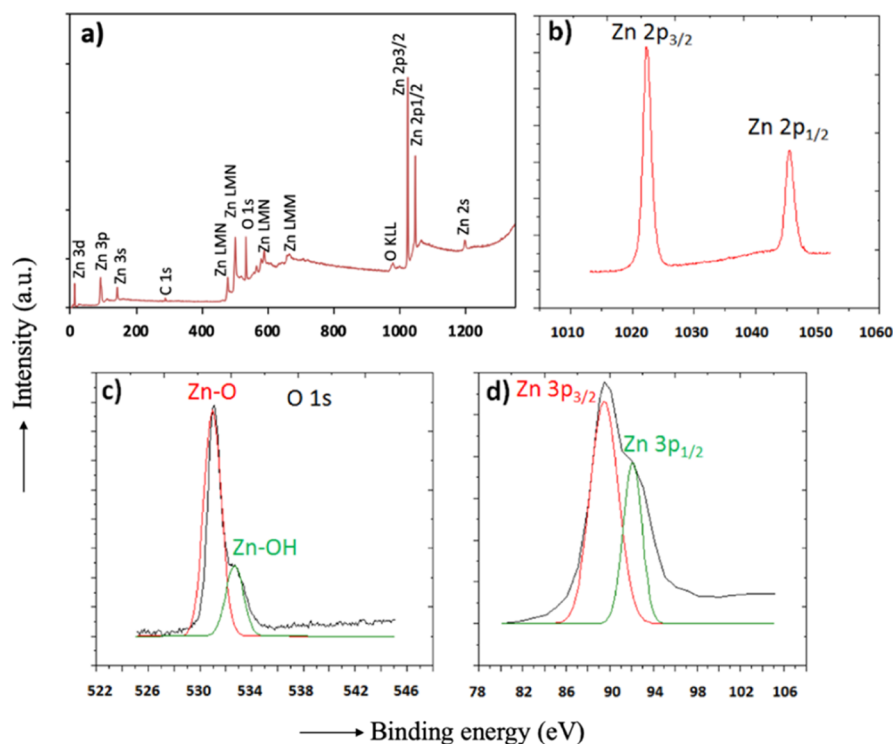


Figure 6. (a) XPS survey spectrum of the nZnO, and high-resolution XPS spectrum of the (b) Zn 2p, (c) O 1s, and (d) Zn 3p electrons.

diameter of the nZnO were measured to be about $0.098 \text{ cm}^3/\text{g}$ and 54.48 \AA , respectively.

3.4. UV–Visible and FTIR Spectrum of the nZnO. The UV–vis spectrum of the nZnO suspension in ethanol (0.125 mg/mL) and the nZnO thin film on the glass substrate is shown in Figure 5a. The nZnO in suspension and in the form of thin film generated similar UV–vis absorption spectrum. In both cases, a sharp absorption band centered at 375 nm was obtained. The absorption band at 375 nm is characteristic to the intrinsic band gap absorption of the nZnO because of the excitation of electrons from the valence band to the CB ($\text{O } 2\text{p} \rightarrow \text{Zn } 3\text{d}$).⁵⁹ On the basis of the absorption band at 375 nm , the band gap energy was calculated according to eq 4.

$$E = hc/\lambda \quad (4)$$

where E is the energy (J), h is Planck's constant ($h = 6.626 \times 10^{-34} \text{ J s}$), c is the speed of light ($2.998 \times 10^8 \text{ m s}^{-1}$), and λ is the wavelength of the maximum absorption (375 nm).^{60,61}

A band gap energy of 3.32 eV was obtained for the nZnO, which is similar to the band gap energy of the zinc oxide reported elsewhere.^{62,63} Moreover, Figure 5a shows that there are significant absorptions in the visible range and an absorption tail reaching to 800 nm . The origin of this absorption and tail could be assigned to the scattering of the light by nZnO in colloidal suspension or in the thin film. Therefore, from the UV–vis spectrum, it is confirmed that the nZnO has a high absorption coefficient in the UV region ($<400 \text{ nm}$) of the electromagnetic radiation.

The FTIR spectra of the nZnO are shown in Figure 5b. A strong peak at 415 cm^{-1} was observed, which is characteristic to the Zn–O stretching vibrational mode of the hexagonal ZnO nanoparticles.^{60,64} This further confirms the formation of ZnO nanoparticles by this method. A less intense peak at $\sim 3400 \text{ cm}^{-1}$ can be attributed to the O–H stretching vibrations originated from the chemically bound OH group or the adsorbed moisture on the nZnO surface.

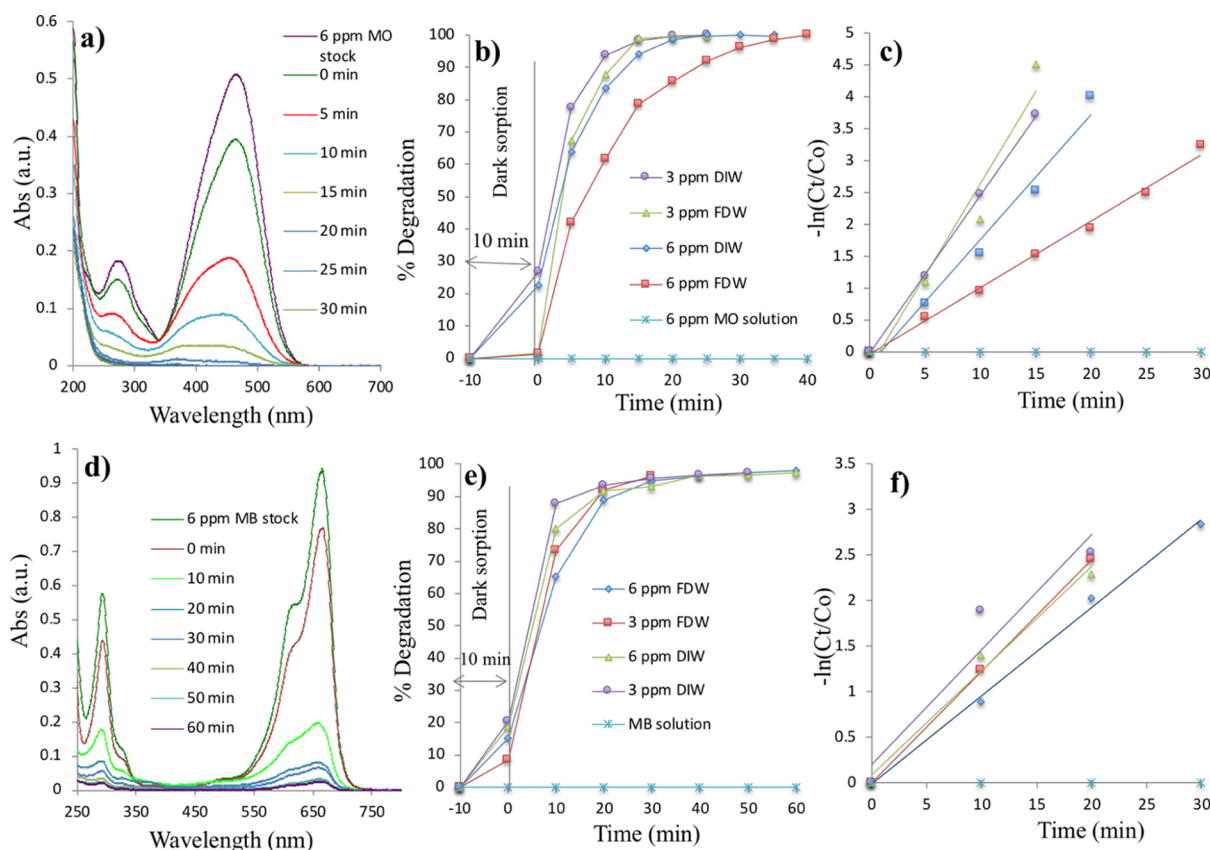


Figure 7. (a,d) Time-dependent UV–vis spectra of the 6 ppm MO and MB solution during the photocatalytic degradation; (b,e) time-dependent percent degradation of MO and MB; and (c,f) pseudo-first-order kinetics of the photocatalytic degradation of MO and MB.

3.5. High-Resolution XPS Analysis of the nZnO. The elemental composition and the purity of the nZnO were characterized by the XPS analysis. From the XPS survey spectrum, it was found that the nZnO was mainly consisting of Zn and O while having a trace of C (Figure 6a). Binding energies characteristic to the ZnO, Zn (2s, 2p, 3s, 3p, 3d), Zn LMM, Zn LMN, O KLL, and O 1s, were observed in the XPS spectrum.^{65,66} The carbon peak may have originated from the adventitious contamination of the XPS instrument.⁵⁴

The Zn 2p_{3/2} and Zn 2p_{1/2} peaks at 1022.5 and 1045.6 eV can be assigned to Zn element in ZnO, respectively.^{54–56} The Zn 3p_{3/2} and Zn 3p_{1/2} binding energy of the nZnO sample can be attributed to the peaks at 88.1 and 91.1 eV, respectively.⁶⁷ The binding energy of O 1s can be attributed to the peak at about 531 eV.^{54,55} The high-resolution XPS spectrum of O 1s can be resolved into two peaks at 531.2 and 532.8 eV, which are characteristic to the Zn–O and the OH on the surface of ZnO, respectively.⁶⁸ The OH group may have originated from the breaking of Zn–O–Zn bond and the formation of Zn–OH bond, during the high-temperature synthesis under the ambient conditions. Therefore, from the XRD and XPS analyses, it could be inferred that the as-synthesized nZnO was highly pure.

3.6. Photocatalytic Degradation of MO and MB by UV Light. The photocatalytic performance of the nZnO was evaluated by the degradation of MO and MB in water under UV and sunlight illumination. As mentioned above, the photocatalysis of MO and MB was done in DIW and simulated FDW matrices. The time-dependent percent degradation of MO and MB was calculated by using eq 5. The UV–visible

spectroscopy was utilized to monitor the degradation of MO and MB.

Percent degradation

$$\begin{aligned}
 &= \frac{C_0 - C_t}{C_0} \times 100\% \\
 &= \frac{A_0 - A_t}{A_0} \times 100\%
 \end{aligned}
 \tag{5}$$

where C_0 and C_t represent the initial and time-dependent concentrations of MO and MB, respectively and A_0 and A_t represent the initial and time-dependent absorbance of MO and MB, respectively.

Figure 7a shows the time-dependent UV–vis spectrum of 6 ppm MO solution in DIW during its photocatalytic degradation in the presence of nZnO. As shown in Figure 7a, the concentration of MO gradually decreased with respect to the time of photocatalysis. The absorption maxima at 464 and 275 nm disappeared almost completely after 30 min of catalysis, which suggested the degradation of MO in water.

The time-dependent percent degradation of 3 and 6 ppm MO solution is shown in Figure 7b. It was found that the 3 ppm MO solution in DIW completely decolorized within 15 min of photocatalysis, whereas it took about 25 min to completely decolorize the 6 ppm MO solution in DIW. It is typical that it takes longer time to degrade pollutants of higher concentration compared to the lower concentration. The percent degradation of MO in FDW was found to be little slower compared to the one in DIW. For example, it took about 40 min to completely degrade the 6 ppm MO solution in

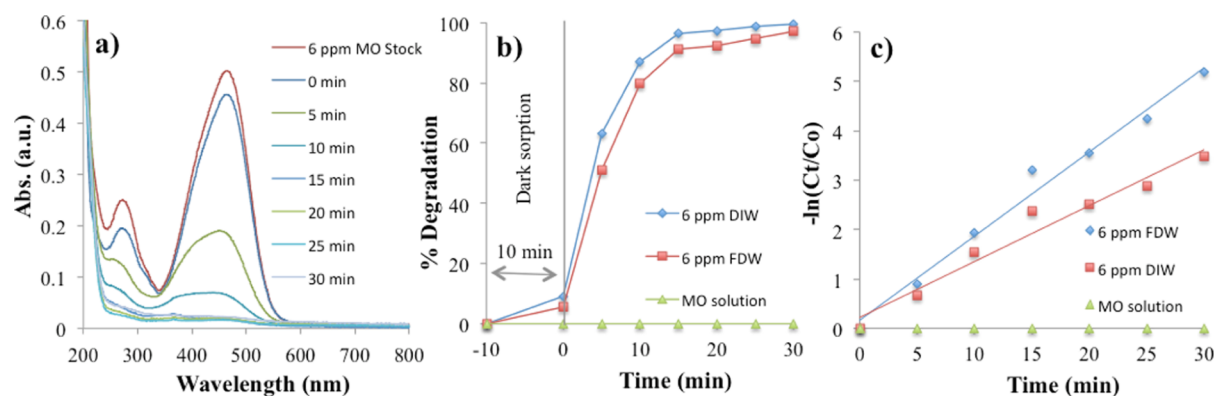


Figure 8. (a) Time-dependent UV–vis spectrum for the photocatalytic degradation of 6 ppm MO in DIW under sunlight irradiation, (b) time-dependent percent degradation of 6 ppm MO solution in DIW and FDW, and (c) pseudo-first-order kinetics of the photocatalytic degradation of MO.

FDW, whereas it took about 25 min in DIW. The presence of dissolved ions could be attributed to this slower photocatalytic activity. Also, it was observed that the extent of MO adsorption was higher in DIW compared to the FDW (Figure 7b). In the absence of the nZnO, the MO solution did not undergo any decolorization under the UV light irradiation, which indicated the robustness of MO against the photodegradation. Moreover, in the absence of light, nZnO showed less than 10% decolorization of the MO solution (6 ppm in DIW) after 30 min (data not shown here), which is mainly due to adsorption. On the other hand, a complete decolorization of MO solution (6 ppm in DIW) was observed after 30 min in the presence of nZnO and UV light (Figure 7b), which indicated that the degradation of MO happened photocatalytically.

The time-dependent UV–vis spectra and the percent degradation of MB are shown in Figure 7d,e, respectively. Both 3 and 6 ppm MB solution show almost complete decolorization in about 30 min period of photocatalysis. The MB solution, in the absence of the nZnO, did not show any degradation under the UV light irradiation. Therefore, it confirmed that the nZnO was responsible for the degradation of MB under the UV light irradiation.

The experimental result for the photocatalytic degradation of MO and MB by nZnO was further analyzed by the pseudo-first-order kinetic model. The pseudo-first-order rate equation is represented as follows

$$kt = -\ln(C_t/C_0) \quad (6)$$

where k represents the rate constant (min^{-1}) of the reaction and C_t and C_0 represent the concentration of the MO and MB at time t and at the beginning of the reaction, respectively.

As shown in Figure 7c,f, the $-\ln(C_t/C_0)$ versus the time (t) graph followed the linear trends, which suggested that the kinetics of the MO and MB degradation followed the pseudo-first-order reaction mechanism. A linear relationship between $-\ln(C_t/C_0)$ and reaction time (t) further indicate that the photocatalytic reaction followed the Langmuir–Hinshelwood model.⁶⁹ The apparent rate constants (k_{app}) of the photocatalytic degradation of MO were calculated to be 2.49×10^{-1} , 1.95×10^{-1} , 2.90×10^{-1} , and $1.04 \times 10^{-1} \text{ min}^{-1}$, respectively, for 3 ppm MO in DIW, 6 ppm MO in DIW, 3 ppm MO in FDW, and 6 ppm MO in FDW solution. Likewise, the rate constants of MB degradation were calculated to be 1.26×10^{-1} , 1.15×10^{-1} , 1.23×10^{-1} , and $9.64 \times 10^{-2} \text{ min}^{-1}$,

respectively, for 3 ppm MB in DIW, 6 ppm MB in DIW, 3 ppm MB in FDW, and 6 ppm MB in FDW solution.

3.7. Photocatalytic Degradation of MO by Sunlight.

The photocatalytic performance of the nZnO was further evaluated by the degradation of 6 ppm MO solution in DIW and FDW by the sunlight irradiation. As shown in Figure 8a–c, the nZnO effectively degraded 6 ppm MO solution in DIW and FDW matrices and the percent degradation reached to almost to 100 within 30 min of sunlight irradiation. The degradation of MO in DIW was found to be faster compared to the FDW matrix (Figure 8b,c). Also, no degradation of MO solution was found in the absence of nZnO. The performance of the nZnO under sunlight irradiation can be attributed to the presence of 4–5% of UV light in solar radiation. Also, the fast-catalytic activity under sunlight irradiation was due to the extremely high intensity of the sunlight in compared to the UV light used in this study. The average intensity of the UV light in the box reactor was about 22 000 lux, whereas the sunlight had an average intensity of about 100 000 lux.

The sunlight irradiated photocatalytic degradation of MO followed the pseudo-first-order reaction kinetics and the rate constants (k_{app}) was calculated to be 1.71×10^{-1} and 1.13×10^{-1} for the 6 ppm MO in DIW and 6 ppm MO in FDW, respectively.

The photocatalytic activity of the nZnO for the degradation of MO and MB, studied in this report, is summarized in Table 1.

Table 1. Photocatalytic Degradation of MO and MB by the nZnO in Different Water Matrices and in Different Types of Light Illumination

pollutants	concentration	water matrix	light source	rate constant (min^{-1})
MO	3 ppm	DIW	UV	2.49×10^{-1}
MO	6 ppm	DIW	UV	1.95×10^{-1}
MO	3 ppm	FDW	UV	2.90×10^{-1}
MO	6 ppm	FDW	UV	1.04×10^{-1}
MB	3 ppm	DIW	UV	1.26×10^{-1}
MB	6 ppm	DIW	UV	1.15×10^{-1}
MB	3 ppm	FDW	UV	1.23×10^{-1}
MB	6 ppm	FDW	UV	9.64×10^{-2}
MO	6 ppm	DIW	sun	1.71×10^{-1}
MO	6 ppm	FDW	sun	1.13×10^{-1}

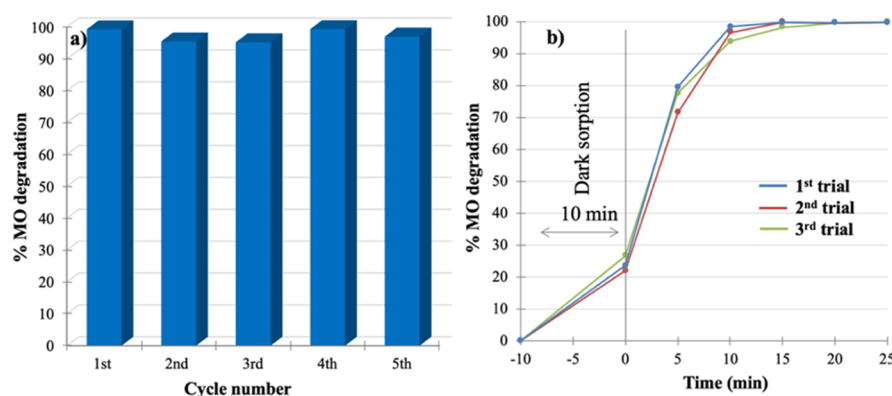


Figure 9. (a) Cyclic stability of the nZnO for 5 cycles of MO degradation and (b) photocatalytic activity of nZnO prepared in three independent trials.

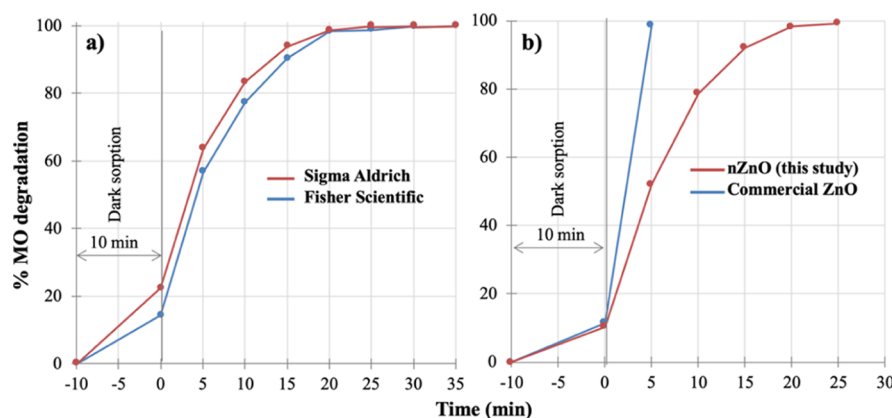


Figure 10. (a) Photocatalytic activity of nZnO prepared from $\text{Zn}(\text{NO}_3)_2 \cdot 6\text{H}_2\text{O}$ obtained from different vendors, viz., Sigma-Aldrich and the Fisher Scientific, and (b) comparison of the photocatalytic activity of the nZnO with the commercial nZnO.

From the above photocatalysis experiments, it could be concluded that the as-prepared nZnO is highly active in the degradation of organic compounds, viz., MO and MB in DIW as well as FDW matrices. Therefore, it could be suggested that the nZnO could effectively be used for the photocatalytic degradation of organic compounds in water by the use of both the UV and the sunlight.

3.8. Cyclic Stability of the nZnO and the Validity of the Method To Prepare nZnO. The cyclic stability of the nZnO was determined by conducting the photocatalytic degradation of MO for 5 cycles over a period of 2 weeks. A mixture of 25 mL of MO solution (6 ppm) and 25 mg of nZnO was irradiated for 30 min under UV light. Afterward, the mixture was centrifuged at 4500 rpm for 10 min to obtain the clear supernatant, which was analyzed by UV–vis spectroscopy to determine the percent degradation of MO. The centrifuged nZnO was used similarly for the following cycles. Figure 9a shows the photocatalytic activity of the nZnO for 5 cycles. The results reveal that the nZnO is fairly active throughout the cycles over the period of study. In every cycle, the nZnO degraded more than 96 percent of the MO. Therefore, from this study, it could be suggested that the nZnO, synthesized in this study, could potentially be utilized as a robust and long lasting photocatalyst for the degradation of organic pollutants from wastewater.

In order to validate the synthesis methodology, the nZnO was prepared in three independent trials that were utilized for the degradation of 6 ppm MO solution in DIW. As can be seen

from Figure 9b, the nZnO prepared in all three trials has the similar activity for the degradation of 6 ppm MO in solution. These results further validated the robustness of the methodology for the synthesis of nZnO.

The robustness of the synthesis methodology was further evaluated by preparing nZnO from zinc nitrate salts obtained from two different vendors, viz., the Sigma-Aldrich and the Fisher Scientific. The nZnO, prepared from the zinc nitrate salts of Sigma-Aldrich and the Fisher Scientific, was utilized for the degradation 6 ppm MO solution in DIW and compared (Figure 10).

It was observed that the nZnO, synthesized from the $\text{Zn}(\text{NO}_3)_2 \cdot 6\text{H}_2\text{O}$ obtained from the Sigma-Aldrich and the Fisher Scientific, had a similar activity for the degradation of 6 ppm MO solution in DIW (Figure 10). Therefore, it could be concluded that a highly photocatalytically active nZnO can be prepared, following the method mentioned in this study, irrespective to the vendors of $\text{Zn}(\text{NO}_3)_2 \cdot 6\text{H}_2\text{O}$. Additionally, the photocatalytic performance of the nZnO, prepared in this study, was compared with the commercially available nZnO obtained from Sigma-Aldrich (Figure 10b). It was found that the photocatalytic activity of the commercial nZnO was much faster compared to the nZnO. The difference in the performance could be because of the difference in the particle size, shape, crystallinity, and the purity of the commercial nZnOs and the nZnO.

3.9. Determination of the ROS Generated in the Photocatalytic Process. The photocatalytic generation of

hydroxyl radicals ($\cdot\text{OH}$) was determined by the TA PL technique.^{70,71} The sodium salt of TA reacts with the photocatalytically generated $\cdot\text{OH}$ to form 2-hydroxyterephthalate, which demonstrate strong fluorescence emission band centered at 425 nm when excited at a wavelength of 315 nm (Figure 11). Qualitatively, the stronger the fluorescence intensity, the higher the amount of the $\cdot\text{OH}$ generation at the interface of water and the catalyst.

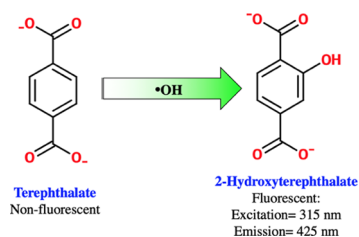


Figure 11. Reaction of terephthalate with the photocatalytically generated $\cdot\text{OH}$ radical to form 2-hydroxyterephthalate.

The results of the TA PL tests are shown in Figure 12. Figure 12a shows the time-dependent fluorescence emission spectrum of 2-hydroxyterephthalate catalyzed by the nZnO, whereas Figure 12b shows the time-dependent fluorescence emission spectrum of 2-hydroxyterephthalate solution under UV light illumination (without the nZnO). For the nZnO catalyzed reaction, it could be seen that the fluorescence emission intensity increased at a much higher rate compared to the uncatalyzed reaction.

Figure 12c shows the fluorescence intensity of 2-hydroxyterephthalate at 425 nm with respect to the time of photocatalytic reaction. It can be seen that the fluorescence intensity for the nZnO catalyzed reaction increased very rapidly up to 10 min and afterward it became slow gradually. The gradual slowing of the fluorescence intensity could be attributed to the gradual decrease in the concentration of TA in the solution and thereby limiting the reaction between the $\cdot\text{OH}$ and the TA. However, at the end of 30 min, the fluorescence intensity was still increasing. In compared to the uncatalyzed reaction, the nZnO catalyzed reaction generated a much higher amount of $\cdot\text{OH}$, which can be seen from Figure

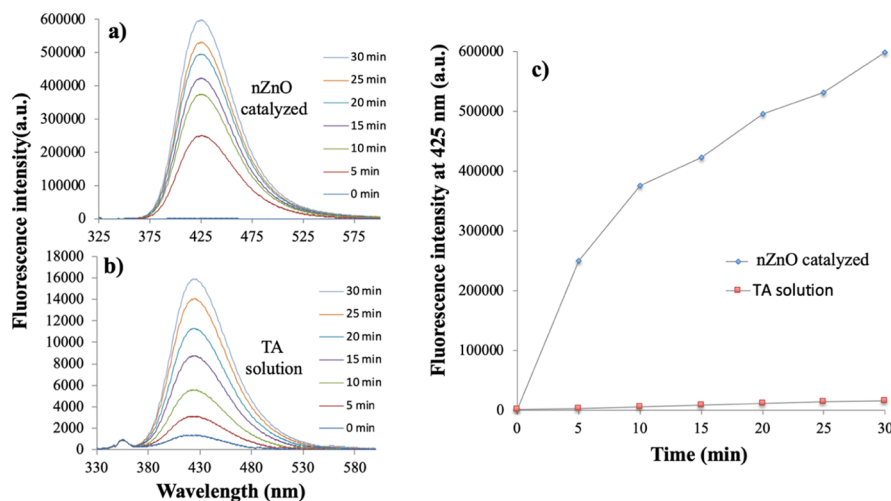


Figure 12. (a) Time-dependent fluorescence spectra of the 2-hydroxyterephthalate solution catalyzed by the nZnO; (b) time-dependent fluorescence spectra of the 2-hydroxyterephthalate solution only (without the nZnO); and (c) fluorescence emission intensity at 425 nm vs graph.

12c. The nZnO catalyzed reaction generated about 38 times more $\cdot\text{OH}$ compared to the uncatalyzed reaction. This result is complying to the photocatalytic degradation of MO and MB that is discussed above. Moreover, the TA fluorescence results indicate that the nZnO can generate hydroxyl radicals under the UV-B light illumination. The photocatalytic generated highly reactive and short-lived $\cdot\text{OH}$ have the ability to nonselectively degrade the organic pollutants in water.

3.10. Proposed Mechanism for the Photocatalytic Degradation of Organic Pollutants. On the basis of the findings of these studies and the results if the previous mechanistic studies, the photocatalytic degradation of organic compounds on nZnO occurs, as shown in Figure 13. The

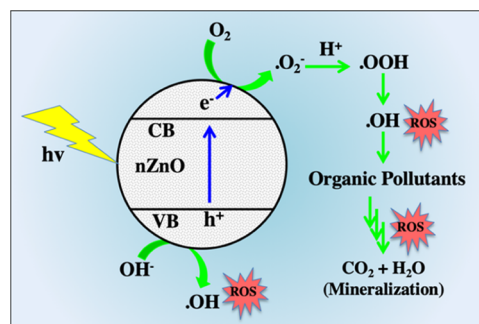


Figure 13. Proposed mechanism for the photocatalytic generation of ROS by the nZnO followed by the degradation of organic pollutants.

photons of the incident light couple with the oscillating valance band (VB) electrons in the nZnO causing the excitation of electrons (e^-) to the CB while leaving holes (h^+) on the VB. These holes (h^+) on the VB then oxidize organic or inorganic species. Holes (h^+) on the VB can also oxidize the hydroxyl (OH^-) ions to hydroxyl radicals ($\cdot\text{OH}$), which can nonselectively and effectively degrade organic pollutants in water.

On the other hand, the excited electrons (e^-) on the CB have the ability to generate ROS [such as superoxide radical anions (O_2^-) and hydroxyl radicals ($\cdot\text{OH}$)] in water. These short-lived, very active, and nonspecific ROS eventually initiate a series of reactions, which can degrade persistent and harmful organic pollutants. The successive degradation of organic

pollutants may lead to the mineralization, which is the formation of harmless gases, viz., CO₂ and H₂O.

4. CONCLUSIONS AND SUMMARY

In conclusion, we report a simple and fast method for the synthesis of nZnO of about 35 nm in size by heating a paste of zinc nitrate hexahydrate and sucrose on the hot plate. The as-prepared nZnO exhibited good photocatalytic activity for the degradation of MO and MB in water. The nZnOs were found to be almost equally active in degrading MO and MB in deionized as well as simulated FDW matrices. The photocatalytic generation of hydroxyl radical was also confirmed by the TA PL tests. The stability of the nZnO was studied for 5 cycles over a period of 2 weeks, which demonstrated no loss of the catalytic activity. The method described in this study can be utilized for the synthesis of nZnO, which in turn could potentially be applied for the photocatalytic degradation of organic pollutants in water. The significance of this report is the simplicity and robustness of the method for the synthesis of nZnO, which could be adapted for the synthesis of a wide variety of other metal and mixed metal oxide nanoparticles for a wide spectrum of applications.

■ AUTHOR INFORMATION

Corresponding Authors

*E-mail: mtislam@miners.utep.edu, tariqul.lab@gmail.com (M.T.I.).

*E-mail: jcnoveron@utep.edu (J.C.N.).

ORCID

Md. Tariqul Islam: 0000-0001-5335-7239

Notes

The authors declare no competing financial interest.

■ ACKNOWLEDGMENTS

Financial support from NSF grants ERC Nanotechnology-Enabled Water Treatment Center 1449500, CHE-0748913, DMR PREM-1205302, and USDA 2014-38422-22078 is gratefully acknowledged. M.O.M. would like to acknowledge the Welch Foundation Chemistry Department Research Grant (AW-0013).

■ REFERENCES

- (1) Djurišić, A. B.; Leung, Y. H.; Ng, A. M. C. Strategies for improving the efficiency of semiconductor metal oxide photocatalysis. *Mater. Horiz.* **2014**, *1*, 400–410.
- (2) Król, A.; Pomastowski, P.; Rafińska, K.; Railean-Plugaru, V.; Buszewski, B. Zinc oxide nanoparticles: Synthesis, antiseptic activity and toxicity mechanism. *Adv. Colloid Interface Sci.* **2017**, *249*, 37–52.
- (3) Wang, Z. L.; Song, J. Piezoelectric nanogenerators based on zinc oxide nanowire arrays. *Science* **2006**, *312*, 242–246.
- (4) Xia, T.; Kovoichich, M.; Liang, M.; Mädler, L.; Gilbert, B.; Shi, H.; Yeh, J. L.; Zink, J. I.; Nel, A. E. Comparison of the mechanism of toxicity of zinc oxide and cerium oxide nanoparticles based on dissolution and oxidative stress properties. *ACS Nano* **2008**, *2*, 2121–2134.
- (5) de Lucas-Gil, E.; Leret, P.; Monte-Serrano, M.; Reinoso, J. J.; Enríquez, E.; Del Campo, A.; Cañete, M.; Menéndez, J.; Fernández, J. F.; Rubio-Marcos, F. ZnO Nanoporous Spheres with Broad-Spectrum Antimicrobial Activity by Physicochemical Interactions. *ACS Appl. Nano Mater.* **2018**, *1*, 3214–3225.
- (6) Raghupathi, K. R.; Koodali, R. T.; Manna, A. C. Size-dependent bacterial growth inhibition and mechanism of antibacterial activity of zinc oxide nanoparticles. *Langmuir* **2011**, *27*, 4020–4028.

- (7) Mitra, P.; Dutta, D.; Das, S.; Basu, T.; Pramanik, A.; Patra, A. Antibacterial and Photocatalytic Properties of ZnO–9-Aminoacridine Hydrochloride Hydrate Drug Nanoconjugates. *ACS Omega* **2018**, *3*, 7962–7970.

- (8) Hosono, E.; Fujihara, S.; Honma, I.; Zhou, H. The fabrication of an upright-standing zinc oxide nanosheet for use in dye-sensitized solar cells. *Adv. Mater.* **2005**, *17*, 2091–2094.

- (9) Chang, C.; Tran, V. H.; Wang, J.; Fuh, Y.-K.; Lin, L. Direct-write piezoelectric polymeric nanogenerator with high energy conversion efficiency. *Nano Lett.* **2010**, *10*, 726–731.

- (10) Lupan, O.; Postica, V.; Gröttrup, J.; Mishra, A. K.; de Leeuw, N. H.; Carreira, J. F. C.; Rodrigues, J.; Sedrine, N. B.; Correia, M. R.; Monteiro, T.; Cretu, V.; Tiginyanu, I.; Smazna, D.; Mishra, Y. K.; Adelung, R. Hybridization of zinc oxide tetrapods for selective gas sensing applications. *ACS Appl. Mater. Interfaces* **2017**, *9*, 4084–4099.

- (11) Dias, H. B.; Bernardi, M. I. B.; Ramos, M. A. d. S.; Trevisan, T. C.; Bauab, T. M.; Hernandez, A. C.; de Souza Rastelli, A. N. Zinc oxide 3D microstructures as an antimicrobial filler content for composite resins. *Microsc. Res. Tech.* **2017**, *80*, 634–643.

- (12) Mirzaei, H.; Darroudi, M. Zinc oxide nanoparticles: Biological synthesis and biomedical applications. *Ceram. Interfaces* **2017**, *43*, 907–914.

- (13) Höfle, S.; Schienle, A.; Bruns, M.; Lemmer, U.; Colsmann, A. Enhanced electron injection into inverted polymer light-emitting diodes by combined solution-processed zinc oxide/polyethylenimine interlayers. *Adv. Mater.* **2014**, *26*, 2750–2754.

- (14) Boruah, B. D.; Misra, A. Energy-efficient hydrogenated zinc oxide nanoflakes for high-performance self-powered ultraviolet photodetector. *ACS Appl. Mater. Interfaces* **2016**, *8*, 18182–18188.

- (15) Sarmah, K.; Roy, U. K.; Maji, T. K.; Pratihar, S. Role of Metal Exchange toward the Morphology and Photocatalytic Activity of Cu/Ag/Au-Doped ZnO: A Study with a Zinc–Sodium Acetate Complex as the Precursor. *ACS Appl. Nano Mater.* **2018**, *1*, 2049–2056.

- (16) Ji, B.; Zhang, J.; Zhang, C.; Li, N.; Zhao, T.; Chen, F.; Hu, L.; Zhang, S.; Wang, Z. Vertically Aligned ZnO@ZnS Nanorod Chip with Improved Photocatalytic Activity for Antibiotics Degradation. *ACS Appl. Nano Mater.* **2018**, *1*, 793–799.

- (17) Trenque, I.; Gaudon, M.; Duguet, E.; Mornet, S. Visible-transparent and UV/IR-opaque colloidal dispersions of Ga-doped zinc oxide nanoparticles. *New J. Chem.* **2016**, *40*, 7204–7209.

- (18) Qi, K.; Cheng, B.; Yu, J.; Ho, W. Review on the improvement of the photocatalytic and antibacterial activities of ZnO. *J. Alloys Compd.* **2017**, *727*, 792–820.

- (19) Daneshvar, N.; Salari, D.; Khataee, A. R. Photocatalytic degradation of azo dye acid red 14 in water on ZnO as an alternative catalyst to TiO₂. *J. Photochem. Photobiol., A* **2004**, *162*, 317–322.

- (20) Jayswal, S.; Moirangthem, R. S. Construction of a solar spectrum active SnS/ZnO p–n heterojunction as a highly efficient photocatalyst: the effect of the sensitization process on its performance. *New J. Chem.* **2018**, *42*, 13689–13701.

- (21) Wang, H.; Qiu, X.; Liu, W.; Yang, D. Facile preparation of well-combined lignin-based carbon/ZnO hybrid composite with excellent photocatalytic activity. *Appl. Surf. Sci.* **2017**, *426*, 206–216.

- (22) Wang, S.; Kuang, P.; Cheng, B.; Yu, J.; Jiang, C. ZnO hierarchical microsphere for enhanced photocatalytic activity. *J. Alloys Compd.* **2018**, *741*, 622–632.

- (23) Zhao, Y.; Cui, T.; Wu, T.; Jin, C.; Qiao, R.; Qian, Y.; Tong, G. Polymorphous ZnO Nanostructures: Zn Polar Surface-Guided Size and Shape Evolution Mechanism and Enhanced Photocatalytic Activity. *ChemCatChem* **2017**, *9*, 3180–3190.

- (24) Yu, W.; Zhang, J.; Peng, T. New insight into the enhanced photocatalytic activity of N-, C- and S-doped ZnO photocatalysts. *Appl. Catal., B* **2016**, *181*, 220–227.

- (25) Islam, M. T.; Jing, H.; Yang, T.; Zubia, E.; Goos, A. G.; Bernal, R. A.; Botez, C. E.; Narayan, M.; Chan, C. K.; Noveron, J. C. Fullerene stabilized gold nanoparticles supported on titanium dioxide for enhanced photocatalytic degradation of methyl orange and catalytic reduction of 4-nitrophenol. *J. Environ. Chem. Eng.* **2018**, *6*, 3827–3836.

- (26) Lu, Z.; Peng, J.; Song, M.; Liu, Y.; Liu, X.; Huo, P.; Dong, H.; Yuan, S.; Ma, Z.; Han, S. Improved recyclability and selectivity of environment-friendly MFA-based heterojunction imprinted photocatalyst for secondary pollution free tetracycline orientation degradation. *Chem. Eng. J.* **2019**, *360*, 1262–1276.
- (27) Bilecka, I.; Niederberger, M. Microwave chemistry for inorganic nanomaterials synthesis. *Nanoscale* **2010**, *2*, 1358–1374.
- (28) Niederberger, M. Nonaqueous sol–gel routes to metal oxide nanoparticles. *Acc. Chem. Res.* **2007**, *40*, 793–800.
- (29) Vafaei, M.; Ghamsari, M. S. Preparation and characterization of ZnO nanoparticles by a novel sol–gel route. *Mater. Lett.* **2007**, *61*, 3265–3268.
- (30) Cao, Y.; Liu, B.; Huang, R.; Xia, Z.; Ge, S. Flash synthesis of flower-like ZnO nanostructures by microwave-induced combustion process. *Mater. Lett.* **2011**, *65*, 160–163.
- (31) Kooti, M.; Sedeh, A. N. Microwave-assisted combustion synthesis of ZnO nanoparticles. *J. Chem.* **2013**, *2013*, 562028.
- (32) Yu, J.; Yu, X. Hydrothermal synthesis and photocatalytic activity of zinc oxide hollow spheres. *Environ. Sci. Technol.* **2008**, *42*, 4902–4907.
- (33) Liu, B.; Zeng, H. C. Hydrothermal synthesis of ZnO nanorods in the diameter regime of 50 nm. *J. Am. Chem. Soc.* **2003**, *125*, 4430–4431.
- (34) Hsieh, S.-H.; Ting, J.-M. Characterization and photocatalytic performance of ternary Cu-doped ZnO/Graphene materials. *Appl. Surf. Sci.* **2018**, *427*, 465–475.
- (35) Mao, Y.; Li, Y.; Zou, Y.; Shen, X.; Zhu, L.; Liao, G. Solvothermal synthesis and photocatalytic properties of ZnO micro/nanostructures. *Ceram. Int.* **2019**, *45*, 1724–1729.
- (36) Amarilio-Burshtein, I.; Tamir, S.; Lifshitz, Y. Growth modes of ZnO nanostructures from laser ablation. *Appl. Phys. Lett.* **2010**, *96*, 103104.
- (37) Park, W. I.; Lee, C.-H.; Chae, J. H.; Lee, D. H.; Yi, G.-C. Ultrafine ZnO nanowire electronic device arrays fabricated by selective metal–organic chemical vapor deposition. *Small* **2009**, *5*, 181–184.
- (38) Li, X.; He, G.; Xiao, G.; Liu, H.; Wang, M. Synthesis and morphology control of ZnO nanostructures in microemulsions. *J. Colloid Interface Sci.* **2009**, *333*, 465–473.
- (39) Komarneni, S.; Bruno, M.; Mariani, E. Synthesis of ZnO with and without microwaves. *Mater. Res. Bull.* **2000**, *35*, 1843–1847.
- (40) Salah, N.; Habib, S. S.; Khan, Z. H.; Memic, A.; Azam, A.; Al-Hamed, E.; Zahed, N.; Habib, S. High-energy ball milling technique for ZnO nanoparticles as antibacterial material. *Int. J. Nanomed.* **2011**, *6*, 863.
- (41) Aruna, S. T.; Mukasyan, A. S. Combustion synthesis and nanomaterials. *Curr. Opin. Solid State Mater. Sci.* **2008**, *12*, 44–50.
- (42) Morales, W.; Cason, M.; Aina, O.; de Tacconi, N. R.; Rajeshwar, K. Combustion synthesis and characterization of nanocrystalline WO₃. *J. Am. Chem. Soc.* **2008**, *130*, 6318–6319.
- (43) Naik, M. A.; Mishra, B. G.; Dubey, A. Combustion synthesized WO₃–ZrO₂ nanocomposites as catalyst for the solvent-free synthesis of coumarins. *Colloids Surf., A* **2008**, *317*, 234–238.
- (44) Ramasami, A. K.; Ravishankar, T. N.; Nagaraju, G.; Ramakrishna, T.; Teixeira, S. R.; Balakrishna, R. G. Gel-combustion-synthesized ZnO nanoparticles for visible light-assisted photocatalytic hydrogen generation. *Bull. Mater. Sci.* **2017**, *40*, 345–354.
- (45) Peralta-Videa, J. R.; Huang, Y.; Parsons, J. G.; Zhao, L.; Lopez-Moreno, L.; Hernandez-Viezas, J. A.; Gardea-Torresdey, J. L. Plant-based green synthesis of metallic nanoparticles: scientific curiosity or a realistic alternative to chemical synthesis? *Nanotechnol. Environ. Eng.* **2016**, *1*, 4.
- (46) Wang, C.; O'Connell, M. J.; Chan, C. K. Facile one-pot synthesis of highly porous carbon foams for high-performance supercapacitors using template-free direct pyrolysis. *ACS Appl. Mater. Interfaces* **2015**, *7*, 8952–8960.
- (47) Becheri, A.; Dürr, M.; Lo Nostro, P.; Baglioni, P. Synthesis and characterization of zinc oxide nanoparticles: application to textiles as UV-absorbers. *J. Nanopart. Res.* **2008**, *10*, 679–689.
- (48) Liu, X.; Chen, N.; Xing, X.; Li, Y.; Xiao, X.; Wang, Y.; Djerdj, I. A high-performance n-butanol gas sensor based on ZnO nanoparticles synthesized by a low-temperature solvothermal route. *RSC Adv.* **2015**, *5*, 54372–54378.
- (49) Mudusu, D.; Nandanapalli, K. R.; Dugasani, S. R.; Park, S. H.; Tu, C. W. Zinc oxide nanorods shielded with an ultrathin nickel layer: tailoring of physical properties. *Sci. Rep.* **2016**, *6*, 28561.
- (50) Baruah, S.; Thanachayanont, C.; Dutta, J. Growth of ZnO nanowires on nonwoven polyethylene fibers. *Sci. Technol. Adv. Mater.* **2008**, *9*, 025009.
- (51) Pichon, B. P.; Mezy, A.; Tedenac, J.-C.; Tichit, D.; Gérardin, C. A soft chemistry route to prepare hybrid ZnO nanostructured films with a lamellar structure. *New J. Chem.* **2009**, *33*, 2350–2354.
- (52) Kang, H. W.; Leem, J.; Yoon, S. Y.; Sung, H. J. Continuous synthesis of zinc oxide nanoparticles in a microfluidic system for photovoltaic application. *Nanoscale* **2014**, *6*, 2840–2846.
- (53) Ahamed, M.; Akhtar, J.; Kumar, S.; Khan, M.; Ahmad, J.; Alrokayan, S. A. Zinc oxide nanoparticles selectively induce apoptosis in human cancer cells through reactive oxygen species. *Int. J. Nanomed.* **2012**, *7*, 845.
- (54) McLaren, A.; Valdes-Solis, T.; Li, G.; Tsang, S. C. Shape and size effects of ZnO nanocrystals on photocatalytic activity. *J. Am. Chem. Soc.* **2009**, *131*, 12540–12541.
- (55) Bindu, P.; Thomas, S. Estimation of lattice strain in ZnO nanoparticles: X-ray peak profile analysis. *J. Theor. Appl. Phys.* **2014**, *8*, 123–134.
- (56) Patterson, A. L. The Scherrer formula for X-ray particle size determination. *Phys. Rev.* **1939**, *56*, 978–982.
- (57) Bai, S.; Hu, J.; Li, D.; Luo, R.; Chen, A.; Liu, C. C. Quantum-sized ZnO nanoparticles: synthesis, characterization and sensing properties for NO₂. *J. Mater. Chem.* **2011**, *21*, 12288–12294.
- (58) Zhou, C.; Wang, Y.; Du, L.; Yao, H.; Wang, J.; Luo, G. Precipitation Preparation of High Surface Area and Porous Nanosized ZnO by Continuous Gas-Based Impinging Streams in Unconfined Space. *Ind. Eng. Chem. Res.* **2016**, *55*, 11943–11949.
- (59) Zak, A. K.; Abrishami, M. E.; Majid, W. H. A.; Yousefi, R.; Hosseini, S. M. Effects of annealing temperature on some structural and optical properties of ZnO nanoparticles prepared by a modified sol–gel combustion method. *Ceram. Interfaces* **2011**, *37*, 393–398.
- (60) Raja, A.; Ashokkumar, S.; Marthandam, R. P.; Jayachandiran, J.; Khatiwada, C. P.; Kaviyarasu, K.; Raman, R. G.; Swaminathan, M. Eco-friendly preparation of zinc oxide nanoparticles using *Tabernaemontana divaricata* and its photocatalytic and antimicrobial activity. *J. Photochem. Photobiol., B* **2018**, *181*, 53–58.
- (61) Zak, A. K.; Razali, R.; Majid, W. H. B. A.; Darroudi, M. Synthesis and characterization of a narrow size distribution of zinc oxide nanoparticles. *Int. J. Nanomed.* **2011**, *6*, 1399–1403.
- (62) Srikant, V.; Clarke, D. R. On the optical band gap of zinc oxide. *J. Appl. Phys.* **1998**, *83*, 5447–5451.
- (63) Awan, F.; Islam, M. S.; Ma, Y.; Yang, C.; Shi, Z.; Berry, R. M.; Tam, K. C. Cellulose Nanocrystal–ZnO Nanohybrids for Controlling Photocatalytic Activity and UV Protection in Cosmetic Formulation. *ACS Omega* **2018**, *3*, 12403–12411.
- (64) Jan, T.; Iqbal, J.; Ismail, M.; Zakoullah, S. H.; Badshah, N.; Haider, S. Sn doping induced enhancement in the activity of ZnO nanostructures against antibiotic resistant *S. aureus* bacteria. *Int. J. Nanomed.* **2013**, *8*, 3679.
- (65) Krzywiecki, M.; Grządziel, L.; Sarfraz, A.; Iqbal, D.; Szwajca, A.; Erbe, A. Zinc oxide as a defect-dominated material in thin films for photovoltaic applications - experimental determination of defect levels, quantification of composition, and construction of band diagram. *Phys. Chem. Chem. Phys.* **2015**, *17*, 10004–10013.
- (66) Al-Gaashani, R.; Radiman, S.; Daud, A. R.; Tabet, N.; Al-Douri, Y. XPS and optical studies of different morphologies of ZnO nanostructures prepared by microwave methods. *Ceram. Int.* **2013**, *39*, 2283–2292.

(67) Gogurla, N.; Sinha, A. K.; Santra, S.; Manna, S.; Ray, S. K. Multifunctional Au-ZnO plasmonic nanostructures for enhanced UV photodetector and room temperature NO sensing devices. *Sci. Rep.* **2014**, *4*, 6483.

(68) Rakshit, T.; Mondal, S. P.; Manna, I.; Ray, S. K. CdS-Decorated ZnO Nanorod Heterostructures for Improved Hybrid Photovoltaic Devices. *ACS Appl. Mater. Interfaces* **2012**, *4*, 6085–6095.

(69) Verma, S.; Dutta, R. K. Enhanced ROS generation by ZnO-ammonia modified graphene oxide nanocomposites for photocatalytic degradation of trypan blue dye and 4-nitrophenol. *J. Environ. Chem. Eng.* **2017**, *5*, 4776–4787.

(70) Nosaka, Y.; Komori, S.; Yawata, K.; Hirakawa, T.; Nosaka, A. Y. Photocatalytic OH radical formation in TiO₂ aqueous suspension studied by several detection methods. *Phys. Chem. Chem. Phys.* **2003**, *5*, 4731–4735.

(71) Hirakawa, T.; Yawata, K.; Nosaka, Y. Photocatalytic reactivity for O₂⁻ and OH radical formation in anatase and rutile TiO₂ suspension as the effect of H₂O₂ addition. *Appl. Catal., A* **2007**, *325*, 105–111.